

## **Reservoir simulations and feasibility study for seismic monitoring at CaMI.FRS**

Marie Macquet and Don C. Lawton

### **ABSTRACT**

The Containment and Monitoring Institute (CaMI) of CMC Research Institutes Inc., in collaboration with the University of Calgary, has developed a comprehensive Field Research Station (FRS) in southern Alberta, Canada. The purpose of CaMI.FRS is to develop new technologies to prevent and monitor early leakages of a deepest, large-scale CO<sub>2</sub> reservoir. To simulate a leakage, a small amount of CO<sub>2</sub> (< 1000 t/year over 5 years) will be injected at a shallow surface (300 m depth). In this study, we focus the feasibility study of seismic time-lapse monitoring using surface seismic instruments. A part of the feasibility work is also the determination of threshold of CO<sub>2</sub> gas-phase detection at shallow depth.

The first step of the feasibility study is the reservoir simulation. We test here the influence of the maximum bottom-hole pressure (and reservoir temperature) and of the ratio vertical permeability over horizontal permeability on the amount of CO<sub>2</sub> you can inject and on the gas plume shape. The next step is the fluid substitution, necessitated to estimate the variation in elastic parameters induced by the gas injection. We test different methods to compute the bulk modulus of the fluid (Reuss, Voigt, HRV and Brie) and compare their results. We also test the influence of several parameters (matrix bulk modulus, porosity and initial saturated bulk modulus) on the results of the fluid substitution. We finally use a 3D finite difference modeling to simulate the seismic response in the elastic models generated for the baseline, for 1 year of injection and for 5 years of injection.

### **INTRODUCTION**

The storage of CO<sub>2</sub> in geological layers is one of the sustainable and secured solutions for reducing the gas emissions into the atmosphere. Several large-scale projects are now running and are demonstrating the strategy of CO<sub>2</sub> sequestration (for example Sleipner in Norway (Arts et al., 2008), Quest in Canada (Rock et al., 2015)). De-risking this method is a crucial step in CCS (Carbon Capture and Sequestration). It starts by a good characterization of the sub-surface to be sure that the site fills the constraints needed for a secure storage (good reservoir capacity and seal layer, absence of major faults...), going from the study of the well logs to the study of seismic data acquired prior to any injection. Following comes a work of modeling. We need to model at the best the subsurface of the area, particularly the porosity and the permeability, in order to do injection simulations and to model the gas migration into the subsurface. This work helps to plan for example the future survey configurations for the monitoring of the gas plume. The last part of a CO<sub>2</sub> injection and sequestration is the monitoring of the field, thanks to several techniques.

In this work, we present the results of the reservoir simulation and the feasibility study for seismic monitoring for CO<sub>2</sub> sequestration applied on the Field Research Station of the Containment and Monitoring Institute (called CaMI.FRS). In the first part, we present the Field Research Station.

The next part focus on the reservoir simulations. Building a geostatic model of the subsurface and running fluid-flow simulations into it is the next important step. It will give us idea of the amount of the CO<sub>2</sub> we can securely inject as well as of the migration of the gas into the subsurface. The accuracy of the injection simulation will depend on the faithfulness of the geostatic model to the reality and on the good estimation of the not-that-well-know parameters (maximum bottom-hole pressure, vertical permeability for instance).

The next step is the fluid substitution which will give us the variation of elastic parameters (P-wave and S-wave velocities, and density) induced by the CO<sub>2</sub> injection. Once again, the physic behind the fluid substitution is not perfectly known and is based on empirical equations. In this part, we test the effect of different methods of fluid substitution as well as the effect of the input parameters on the variation in P-wave velocity due do gas injection.

In the last part, we present the seismic responses obtained using different sets of elastic models (baseline, after 1 year of injection and after 5 years of injection). This part characterize the feasibility study of using 4D seismic in CaMI.FRS.

### **CAMI.FRS**

The Containment and Monitoring Institute (CaMI) of CMC Research Institutes Inc., in collaboration with the University of Calgary, has developed a comprehensive Field Research Station (FRS) in southern Alberta, Canada (Figure 1).

The purpose of the CaMI.FRS is to simulate a migration of CO<sub>2</sub> in the shallowest part of the subsurface due to a leakage of a deepest large-scale gas reservoir and develop technologies to detect and monitor it. The way to do that is to inject a small amount of CO<sub>2</sub> (around 1.000 ton/year) at shallow depth (300 m) as show on Figure 2.

To detect and monitor the injected CO<sub>2</sub>, different geochemical and geophysical instruments are in place on the field (Lawton et al., 2015b). So far, they are used to characterize the subsurface and will be used as baseline for the monitoring studies. A non-exhaustive list of geophysical instruments on CaMI.FRS includes :

- a Digital Acoustic Sensing (DAS) optical fibre permanently installed (Lawton et al. (2016), Gordon and Lawton (2017), Hall et al. (2017) and Lawton et al. (2017));
- VSP experiments with downhole geophones (Hall et al. (2015) and Gordon et al. (2016));
- surface seismic survey (Isaac and Lawton (2015) and Isaac and Lawton (2017));
- a permanent array of 10x10 geophones (10m spacing, buried at 1m depth) with permanent sources (Lawton et al. (2015a) and Spakman and Lawton (2017)).



FIG. 1. Map of Alberta, Canada showing the location of the Containment and Monitoring Institute Field Research Station (FRS).

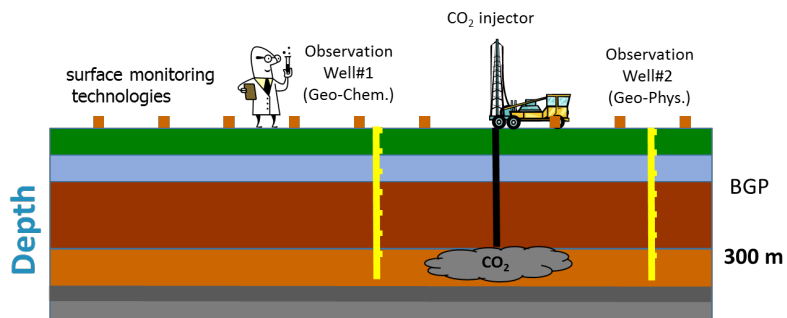


FIG. 2. Schematic 2D view of CaMI.FRS.

A stratigraphic column of CaMI.FRS is presented on Figure 3. The injection target is the Belly Basal River Sandstone (BBRS). It is a 7m layer thickness (from 295 to 302m depth), composed of fine to medium-grained of poorly to well sorted sandstone (see Figure 4 on the right). The seal formation is the Foremost Fm which is the 152m thickness layer composed of clayey sandstone with more or less continuous coal layers (see Figure 4 on the left).

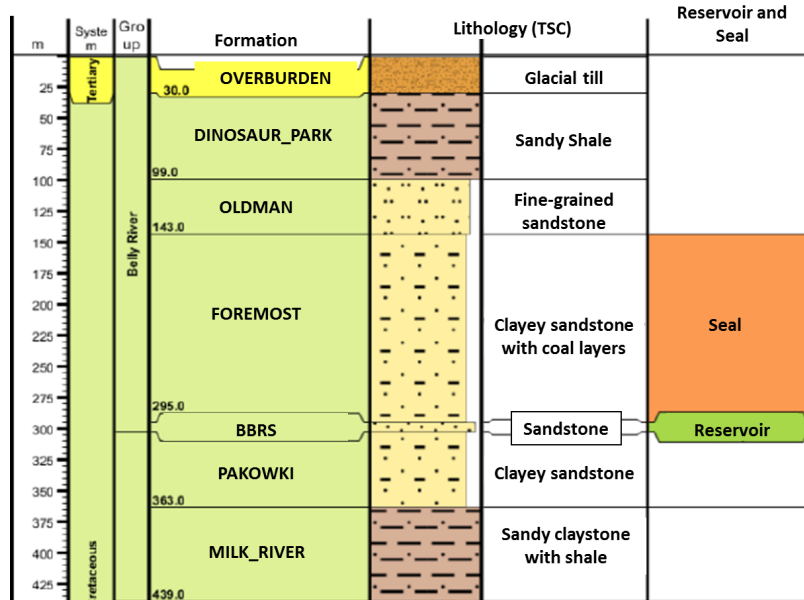


FIG. 3. Stratigraphic succession in the CMCRI Countess #1 Well (injection well, kb 784.5m).

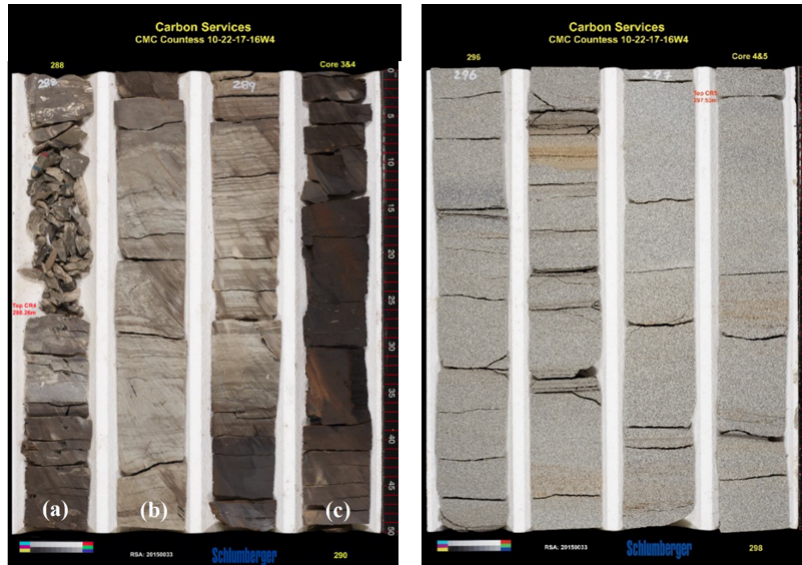


FIG. 4. Photos of the slabbed core interval. Left: Foremost formation (cap-rock) unit from 288 to 299m depth. Right: BBRS (target layer) unit from 296 to 298m depth.

## RESERVOIR SIMULATIONS

Reservoir simulation is an essential step in CO<sub>2</sub> storage to try to understand the behavior of the gas injection. The very first step is to build the most accurate geostatic model possible and then test the different injection scenarios in that model. We will here summarize the work done so far on that subject but a whole review can be found in Saefar et al. (in prep.).

### Geostatic model

The geomodeling work was made by J. Dongas (Dongas, 2016) and then upgraded by J. Barraza (Barraza, 2016). Build a geomodel is always an on-going work as the model is updated when new data acquired. It is also supposed to be updated once the injection start as the data acquired during the injection (as pressure, temperature and geophysics responses) may provide information on the reservoir response to the gas injection.

The geostatic models were build using :

- logs from 88 wells available in the area (including the injection well and the two monitoring wells).
- two seismic volumes
  - Cenovus-1997: A 30km<sup>2</sup> 3D regional survey acquired in 1997 by Cenovus.
  - CMC-2014: A 1km<sup>2</sup> higher resolution 3D seismic survey collected in 2014 by CMC.

Different geostatic models were build, without or with lateral variation, using only the injection well or using all the wells (Zaluski et al., 2016). Based on their initial work on flow simulation on these models, we choose to work with the layer cake, homogeneous model. Indeed, it was demonstrated that the amount of CO<sub>2</sub> injected and the plume shape was not very different using the different models.

Figure 5 shows a zoom of the 3D geostatic model used for the simulation injection. The average porosity for the reservoir is  $\approx 10\%$  and the average horizontal permeability is  $\approx 0.8\text{mD}$ . The lithology obtained along the injector well (Swager, 2015) is also added on Figure 5. We can notice that the low porosity layers correspond to the layers with a high content of coal. The permeability of the geostatic model is based on the mineralogy (for example illite has a low permeability), the grain size, the pore geometry, the pore connectivity but also on the part of free or irreducible water which fills the porosity (see Dongas (2016) for a full discussion on the calculation of porosity and permeability).

Note that the resolution is not the same for all the plots. The porosity and horizontal permeability extracted from the geostatic model has a vertical resolution of 0.5 m in the BBRs unit and increase from 0.5 to 51 m on the over and underlying layers, depending of the distance of the BBRs. The lithology extract from the ELAN logs has a resolution of 0.15 m.

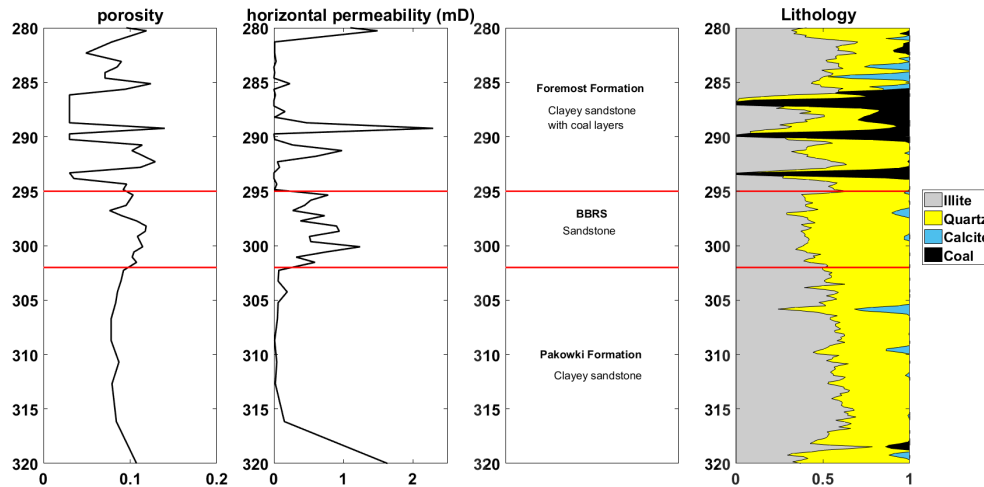


FIG. 5. Zoom in the are of interest of the layer cake model without lateral variation. The porosity and the permeability are extracted from the 3D geostatic models. The lithology is extracted from the ELAN logs (Swager, 2015). Red lines are the limits of the BBRS which is the layer of injection.

### Tests on injection simulations

We test different scenarios of injection using the layer cake model without structural variation presented in the last section. The geostatic model is exactly the same (same horizontal permeability and same porosity) for the different tests, as well as the minimum water saturation (0.5) and the relative permeability of gaseous  $\text{CO}_2$  and water (calculated using Brooks-Corey approximation). We also assumed a initial saturation of brine of 100% in the medium. The different tests were made using GEM, which is the fluid flow simulator of CMG.

#### *Influence of the maximum bottom hole pressure*

We first test the influence of the maximum bottom-hole pressure. We consider a continuous injection over 5 years. The fluid flow simulator software injects the maximum  $\text{CO}_2$  in the medium, without over passing the maximum bottom hole pressure choose. One of the main challenge of CaMI.FRS is the low pressure and temperature of the medium, because of the shallow depth of injection. The fracture pressure (or lithostatic pressure) is estimated to be 6.62 MPa at 300 m depth. For regulatory reason and to conserve the integrity of the cap-rock, the maximum bottom hole pressure has to be inferior to 90% of the fracture pressure. Considering this constrain, we also want the  $\text{CO}_2$  remains in gaseous phase. Figure 6 shows the 6 different injection parameters used in this section (from [BHP=4.8 MPa; T=12.8°C] to [BHP=5.8 MPa; T=20°C]). The temperature was choose to be the highest possible, but remaining in gaseous phase.

Figure 7 shows the injection rate and the cumulative gas for the different cases (shown on Figure 6). Table 1 resumes the value of this parameters for the different scenarios of injection. Instinctively, the highest the maximum bottom hole pressure is, the more you can inject gas. It can also be seen on the size of the  $\text{CO}_2$  plume (Table 1), which is bigger when you increase the maximum bottom-hole pressure.

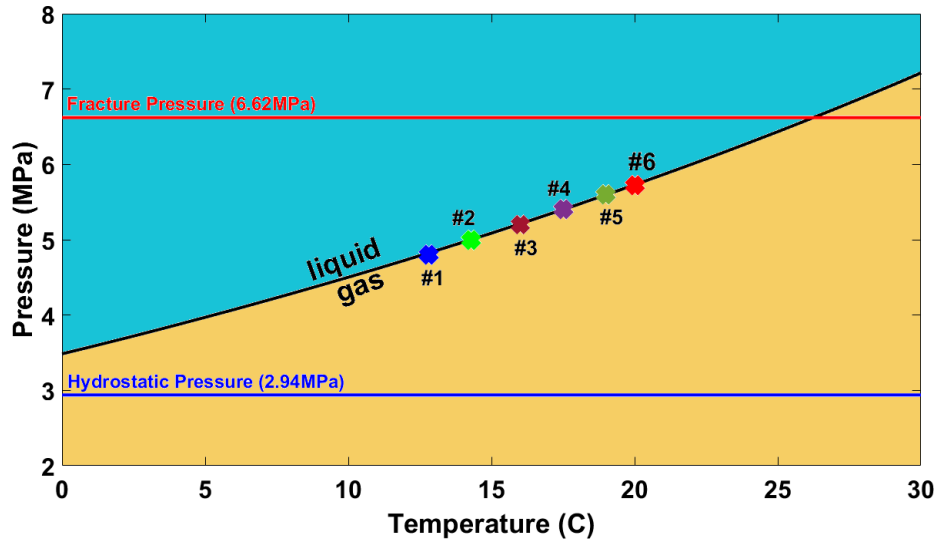


FIG. 6. CO<sub>2</sub> pressure-temperature physical phase diagram. The crosses are the 6 different cases tested in this section.

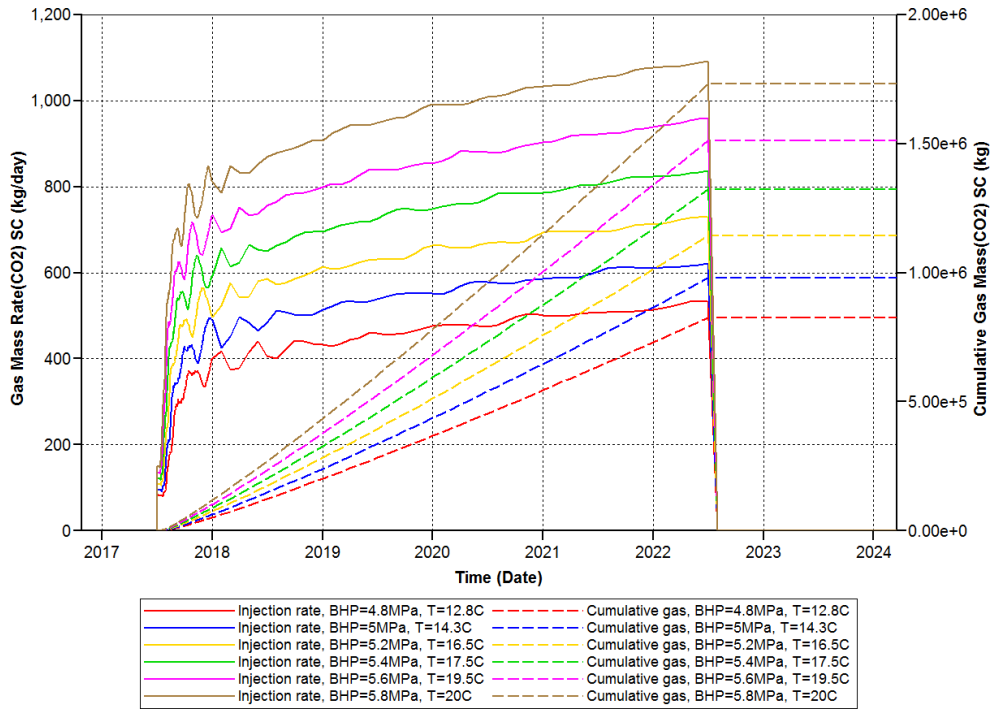


FIG. 7. Injection rate (kg/day) and cumulative gas (kg) for different maximum bottom hole pressure.

We can note on Figure 7 than the injection rate does not reach its maximum value during the first year. It first increases during the first 3 months, then fluctuate before stabilize after 1 year of injection.

Table 1. Average injection rate, total gas injected and lateral expansion of the plume as a function of maximum bottom-hole pressure.

Max BHP MPa	T °C	average injection kg/day	total gas injected tons	plume radius 1 year injection (m)	plume radius 5 years injection (m)
4.8	12.8	450	825	30	80
5	14.3	535	980	40	95
5.2	16.5	630	1145	40	100
5.4	17.5	725	1320	45	100
5.6	19.5	835	1520	50	110
5.8	20	950	1730	50	115

*Influence of the vertical permeability*

An other important parameter is the vertical permeability of the medium. This parameter play a role in the ability for the CO<sub>2</sub> to migrate vertically. However, if we have access to the horizontal permeability (from the well logs), we don't have actual data for the vertical permeability. The ratio vertical to horizontal permeability ( $k_v/k_h$ ) commonly used in the Alberta Basin is 0.1, so the flow of the CO<sub>2</sub> is mainly in the horizontal directions. We test here different values for  $k_v/k_h$ : 0.1, 0.2, 0.3, 0.4, 0.5, 0.75, 1. We also test the injection for a random value of  $k_v/k_h$ , between 0 and 0.2, with an average of 0.08 in the reservoir target. All the other parameters remain the same.

Figure 8 sows the injection rate and cumulative gas for the different values of  $k_v/k_h$ . We can see that the higher the  $k_v/k_h$  is, the more CO<sub>2</sub> you can inject.

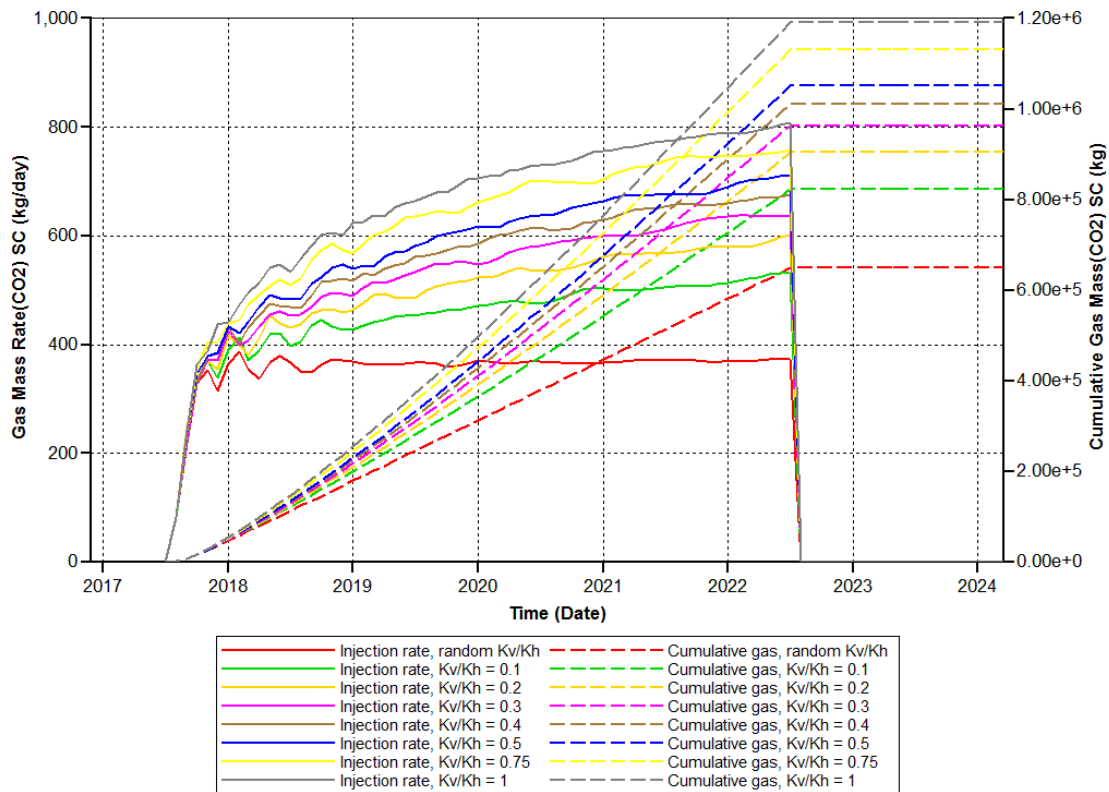


FIG. 8. Injection rate (kg/day) and cumulative gas (kg) for different  $k_v/k_h$ .

Figure 9 shows the CO<sub>2</sub> plume expansion after 5 years of injection, for the different value of  $k_v/k_h$  used. We can see that the higher the ratio  $k_v/k_h$  is, the more the gas is allowed to migrate vertically (plume maximal vertical expansion goes from 11 m for  $k_v/k_h = 0.1$  to 24.5 m for  $k_v/k_h=1$ ). If more gas is allowed to migrate vertically, the pressure decrease in the cell, we can inject more CO<sub>2</sub> and so the injection rate and total gas injected is higher (see Figure 8). However, we can see that the vertical upward migration is still almost non-existent due to the very low permeability of the coal layer at the bottom of the Foremost Formation (see Figure 5).

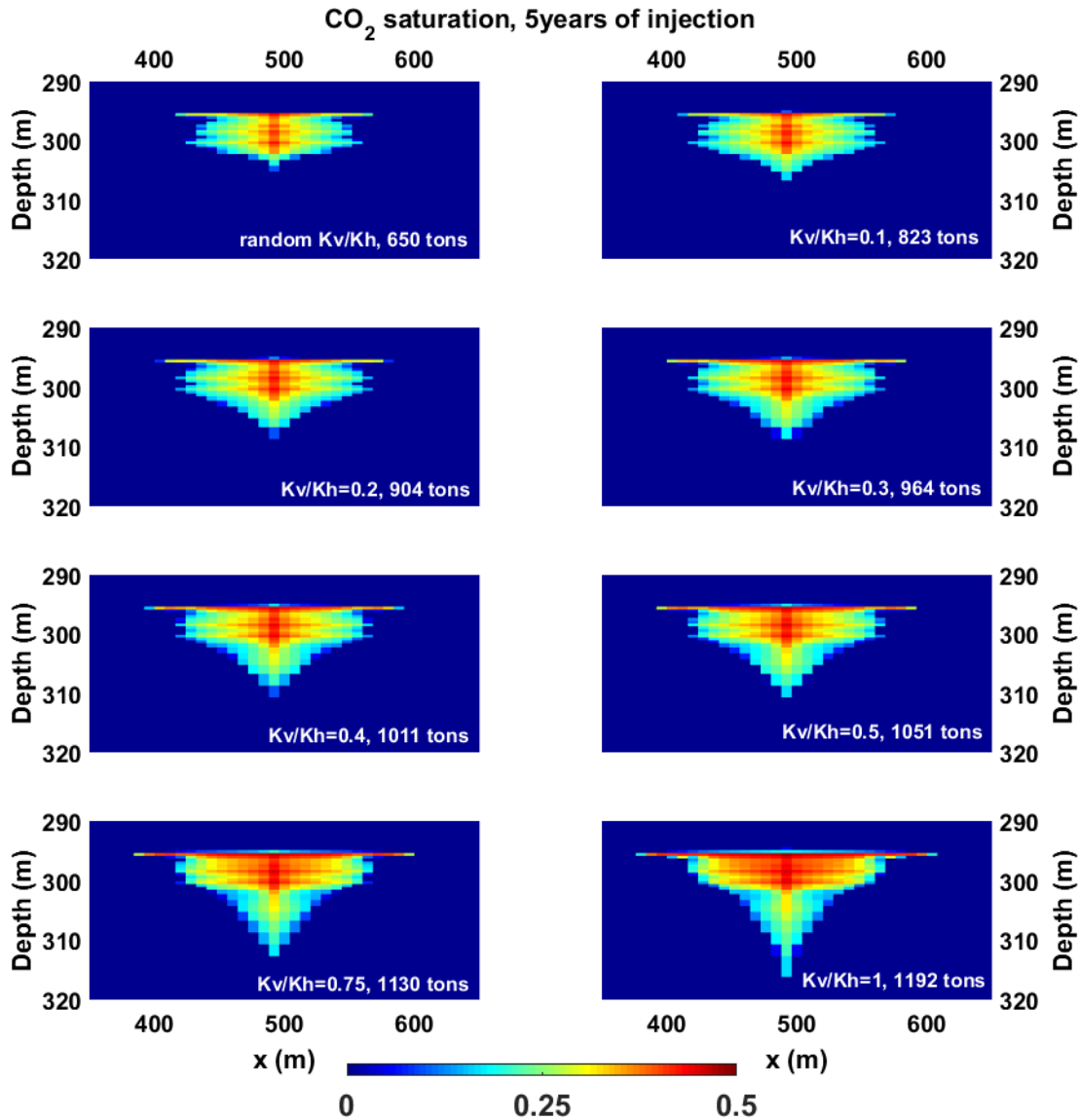


FIG. 9. CO<sub>2</sub> saturation for different  $k_v/k_h$ .

## Final results

We present here the results of the injection simulations we use in the following parts of the report. They are obtained using a maximum bottom hole pressure of 5.8MPa and a reservoir temperature of 20°C. Using this scenario, we can inject a total amount of 1330 tons of CO<sub>2</sub> over the whole period of 5 years. Figure 10 shows the CO<sub>2</sub> saturation for different times: 1 year of injection (266 tons of CO<sub>2</sub>), 5 years of injection (1330 tons of CO<sub>2</sub>), 1 year post closure, and 5 years post closure. The white lines represent the limits of the BBRs which is the zone of injection. We can see that we have a small downward migration ( $\approx 3\text{m}$ ) in the Pakowki Formation but no upward migration in the Foremost Formation.

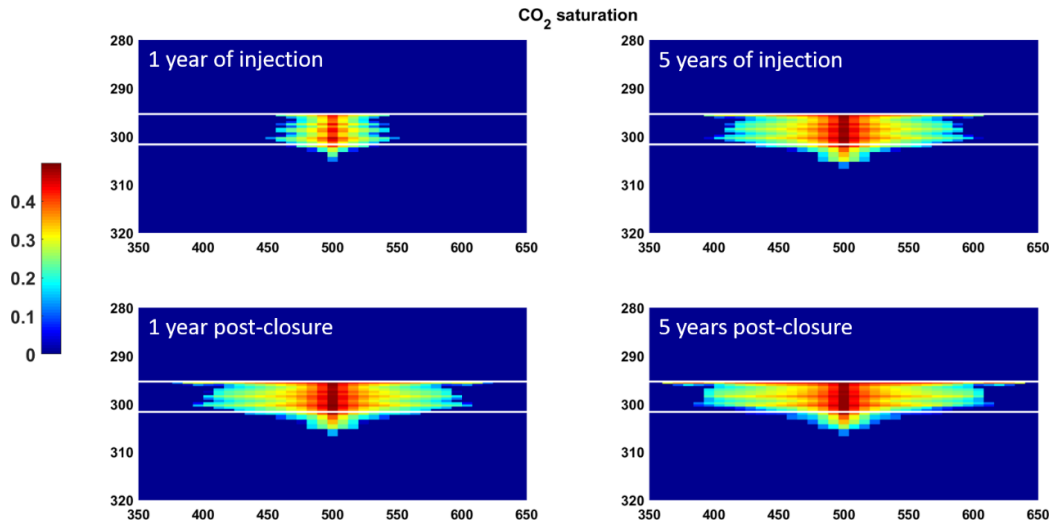


FIG. 10. CO<sub>2</sub> saturation during and after the injection program. a) after 1 year of injection, b) after 5 years of injection, c) after 1 year post-closure, d) after 5 years post-closure. The top and bottom of the BBRs are shown by the white lines.

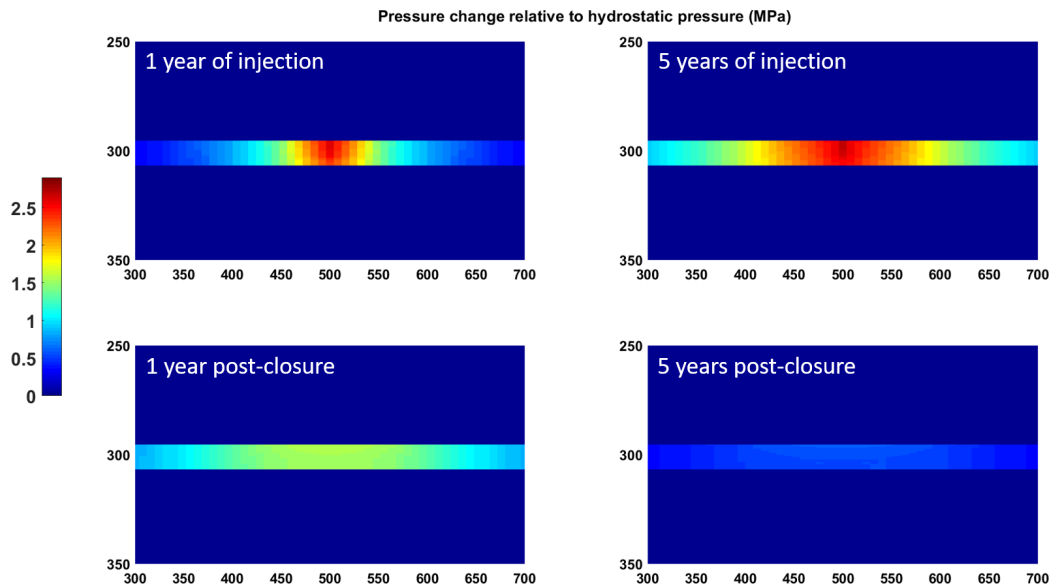


FIG. 11. Pressure changes relative to baseline reservoir pressure due to gas-phase CO<sub>2</sub> injection. a) after 1 year of injection, b) after 5 years of injection, c) after 1 year post-closure, d) after 5 years post-closure.

Figure 11 shows the pressure built-up for the same periods of time than Figure 10. The hydrostatic pressure at 300 m is 2.94 MPa. We can see that after the end of the injection, pressure is quickly released (Figure 11.c) and we almost reach the hydrostatic pressure 5 years post-closure (Figure 11.d).

## FLUID SUBSTITUTION

### Theory

The fluid substitution is used to compute the new elastic parameters as the response to the fluid injection (equations 1-3).

$$\rho_{new} = \rho_{matrix}(1 - \phi) + \rho_{fl_{new}}\phi \quad (1)$$

$$V_{P_{new}} = \sqrt{\frac{K_{sat_{new}} + \frac{4}{3}\mu_{sat}}{\rho_{new}}} \quad (2)$$

$$V_{S_{new}} = \sqrt{\frac{\mu_{sat}}{\rho_{new}}} \quad (3)$$

The new density (eq. 1) can be easily compute as it is a function of the porosity, the matrix density and the density of the fluid in the medium (which is the arithmetic average of the density of the brine and CO<sub>2</sub> which composed the fluid). The shear bulk modulus ( $\mu_{sat}$ ) in equations 2 and 3 remains the same before and after injection and is computed using equation 4.

$$\mu_{sat} = \mu_{init} = \rho_{init}V_{S_{init}}^2 \quad (4)$$

We used the Gassman's equation (eq. 5, Gassmann (1951)) to compute the new saturated bulk modulus ( $K_{sat_{new}}$ ) used to calculate the new P-wave velocity (eq. 2).

$$K_{sat} = K^* + \frac{[1 - (\frac{K^*}{K_0})]^2}{\frac{\phi}{K_{fl}} + \frac{(1-\phi)}{K_0} - \frac{K^*}{K_0^2}} \quad (5)$$

where  $K_{sat}$  is the saturated bulk modulus ;  $K^*$  the frame bulk modulus (or bulk modulus of the porous rock frame, drained of any pore-filling fluid) ;  $K_0$  the bulk modulus of the mineral matrix ;  $\phi$  the porosity and  $K_{fl}$  the bulk modulus of the fluid.

The frame bulk modulus can be obtained by the Gassmann equation and be express as in equation 6.

$$K_{init}^* = \frac{K_{sat_{init}} \left( \frac{\phi K_0}{K_{fl_{init}}} + 1 - \phi \right) - K_0}{\frac{\phi K_0}{K_{fl_{init}}} + \frac{K_{sat_{init}}}{K_0} - 1 - \phi} \quad (6)$$

This parameter does not vary regarding to the fluid in the system, in other words  $K_{init}^* = K_{new}^*$ . This can be used to re-arranged the Gassmann's equation into equation 7.

$$K_{sat_{new}} = \frac{K_0}{\left[ \frac{K_{sat_{init}}}{K_0 - K_{sat_{init}}} - \frac{K_{fl_{init}}}{\phi(K_0 - K_{fl_{init}})} + \frac{K_{fl_{new}}}{\phi(K_0 - K_{fl_{new}})} \right]^{-1} + 1} \quad (7)$$

In equation 7, the porosity  $\phi$  comes from the geostatic model (Figure 5), the matrix bulk modulus  $K_0$  is obtained using equation 8, the initial saturated bulk modulus  $K_{sat_{init}}$  is obtained with the initial elastic parameters using equation 11 and the computation of fluid bulk modulus  $K_{fl_{init}}$  and  $K_{fl_{new}}$  is explained in the next part.

$$K_0 = \frac{1}{2} [K_{Reuss} + K_{Voigt}] \quad (8)$$

where  $K_{Reuss}$  and  $K_{Voigt}$  are calculated using equations 9 and 10.

$$K_{Reuss} = \left[ \sum_{i=1}^n \frac{V_i}{K_i} \right]^{-1} \quad (9)$$

$$K_{Voigt} = \sum_{i=1}^n V_i K_i \quad (10)$$

$$K_{sat_{init}} = \rho_{init} \left( V_{P_{init}}^2 - \frac{4}{3} V_{S_{init}}^2 \right) \quad (11)$$

#### Note on the fluid bulk modulus

The fluid bulk modulus is a combination of the bulk modulus and the saturation of each component composing the fluid. In this study, we only consider the fluid be composed by the initial brine ( $K_{brine}$ , saturation  $S_{brine}$ ) and the  $CO_2$  injected ( $K_{CO_2}$ , saturation  $S_{CO_2}$ ). Depending of how patchy or uniform you consider the saturation, we can express the fluid bulk modulus using different methods: Reuss (harmonic average), Voigt (arithmetic average), HRV (average of Reuss and Voigt) or Brie (equations 12 - 15).

$$K_{fl_{Reuss}} = \left[ \frac{S_{brine}}{K_{brine}} + \frac{S_{CO_2}}{K_{CO_2}} \right]^{-1} \quad (12)$$

$$K_{fl_{Voigt}} = S_{brine} * K_{brine} + S_{CO_2} * K_{CO_2} \quad (13)$$

$$K_{fl_{HRV}} = \frac{1}{2} [K_{fl_{Reuss}} + K_{fl_{Voigt}}] \quad (14)$$

$$K_{fl_{HRV}} = (K_{brine} - K_{CO_2}) S_{brine}^m + K_{CO_2} \quad (15)$$

where  $m$  is an empirical parameter. If  $m=1$ , eq.15 gives eq.13, if  $m=40$ , eq.15 approximates eq.12. Carcione et al. (2006) propose  $m=5$  to obtain good agreement with experimental results of Johnson (2001). We will use this equation for the application of the fluid substitution.

Figure 12 shows the fluid bulk modulus computed using the different equations. The Reuss method corresponds to a uniform saturation, Voigt method corresponds to a patchy saturation, HRV correspond to a semi-patchy saturation.  $K_{brine}$  and  $K_{CO_2}$  are computed using Watzle and Wang equations (Batzle and Wang, 1992), for reservoir conditions (depth=300 m, pressure=2.65 GPa and temperature = 20°). For these conditions, the bulk modulus of the  $CO_2$  is 0.102 GPa and the bulk modulus of the brine is 2.232 GPa.

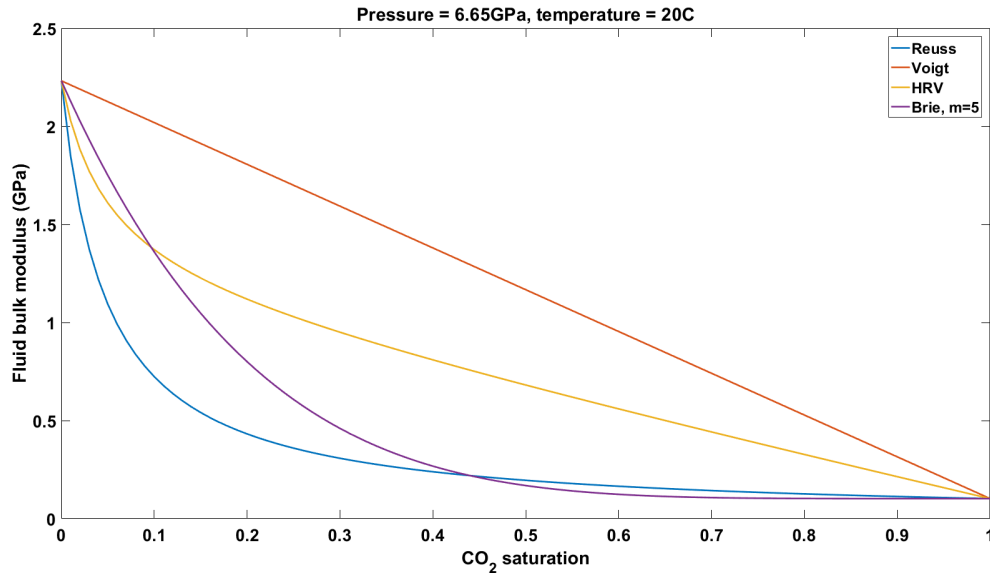


FIG. 12. Fluid bulk modulus for the different methods of calculation.

## Application of fluid substitution

### Input data

Figure 13 shows the 1D profiles used as input for the fluid substitution, with the well logs discretization and the 1m thickness discretization. The initial elastic parameters come from the  $V_P$ ,  $V_P/V_S$  and  $\rho$  logs of the injection well. Mineral volume fraction (Quartz, Illite, Calcite, and Coal) come from the ELAN (ELEMENTAL ANALYSIS) of the well logs.

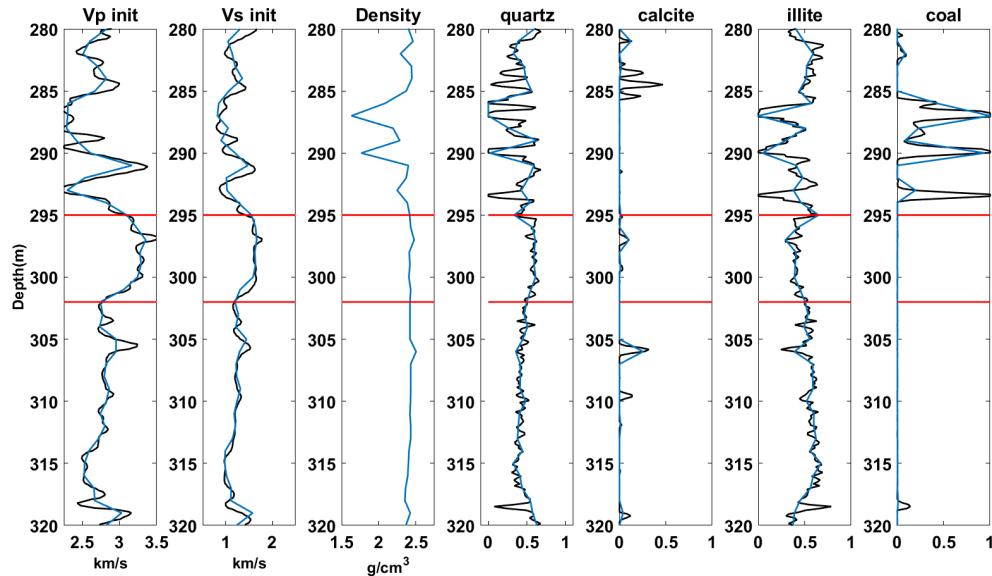


FIG. 13. Zoom in the 1D profiles used as input for the fluid substitution. Red lines show the injection layer (BBRS). Black lines are well logs vertical discretization, blue lines are 1m thickness discretization.

In addition, the porosity model extracted from the geostatic model (Figure 5) is used as well as the gas saturation and pressure response obtained during the fluid-flow simulations (Figures 10 and 11).

#### *Influence of $K_0$ , $K_{sat_{init}}$ and the porosity on $\Delta V_P$*

The initial bulk modulus, the porosity, the matrix bulk modulus and the fluid bulk modulus are the parameters useful to compute the new saturated bulk modulus (eq. 7). The matrix bulk modulus ( $K_0$ ) is coming from the average between the Reuss and the Voigt bulk modulus (which are function of the volumetric fraction and the bulk modulus of each mineral composing the matrix (equation 8)). The initial saturated bulk modulus is computed using the initial elastic parameter (equation 11). The porosity is extracted from the geostatic model. We use equations 12 or 15 to compute the fluid bulk modulus.

Figure 14 shows the 1D profiles of the P-wave velocity variation using the parameters as just described (blue curves) or using the average of these parameters (red curves), and using the Brie equation (continuous curves, eq. 15) or the Reuss equation (dotted curves, eq. 12) to compute the fluid bulk modulus.

The average is computed in the injection layer (average matrix bulk modulus  $K_0 = 22\text{GPa}$ , average porosity  $\phi = 9\%$  and average initial matrix bulk modulus  $K_{sat_{init}} = 25\text{GPa}$ ).

We can see on Figure 14 that if you consider constant initial bulk modulus, porosity and matrix bulk modulus (red curves), the variation in  $V_P$  is perfectly correlated to the  $\text{CO}_2$  plume shape. However, if you consider variable initial bulk modulus, porosity and matrix bulk modulus, the variation in P-wave velocity is not correlated to the gas plume shape but depends of the variable parameters.

The P-wave velocity variation is higher using the Reuss equation to compute the fluid bulk modulus (dotted curve) than using the Brie equation (continuous line). This can be explained because the fluid bulk modulus using Reuss equation is lower than using Brie equation (see Figure 12).

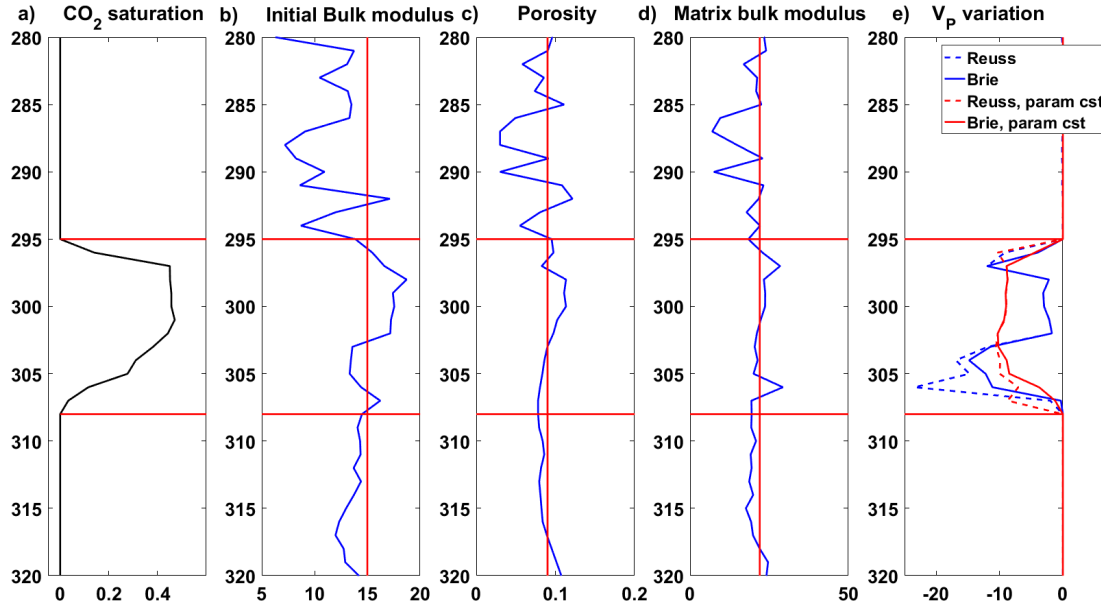


FIG. 14. 1D profiles along the injection well. a)  $\text{CO}_2$  saturation after 5 years of injection. b) Initial bulk modulus, using a constant value in red, using eq. 11 in blue. c) Porosity, using a constant value in red, extracted from geostatic model in blue. d) Matrix bulk modulus, using a constant value in red, using eq. 8 in blue. e) P-wave velocity variations using constant parameters in red, using variable parameters in blue. Continuous curves are using Brie equation to compute fluid bulk modulus (eq. 15), dotted curves are using Reuss equation to compute fluid bulk modulus (eq. 12)

To explain the effect of the effect of the different parameters on the P-wave velocity variation, we made sensitivity tests. Figure 15 shows the influence of parameters ( $K_0$ ,  $K_{sat_{init}}$  and  $\phi$ ) on the variation in P-wave velocity. When one parameter is tested (using a range of value physically compatible with our model), the others two one remains constant.

We can see on Figure 15 that the variation in the porosity has a weak effect on the  $V_P$  variation. The range of variation goes from -0.5 to 1%. The matrix as a greater effect on the P-wave velocity with a range of variation going from -10 to 0%. The variation is equal to 0 if the matrix bulk modulus is equal to the initial bulk modulus. The parameter with the more influence on the variation in  $V_P$  is the initial bulk modulus with variation going from 0 to -40%.

If you consider those three parameters are variable with depth, the resulting variation in P-wave velocity will not be only a function of the  $\text{CO}_2$  saturation but also a function of the initial bulk modulus, the matrix bulk modulus and the porosity.

Considering these sensitivity analyses, we can better understand that the low  $V_P$  variation in the middle of the reservoir (blue curves compare to red curves) is due to a high initial bulk modulus. The high  $V_P$  variation at the bottom of the reservoir is due to a low

initial bulk modulus and a high matrix bulk modulus (due to high concentration of calcite at this depth (see Figure 13)).

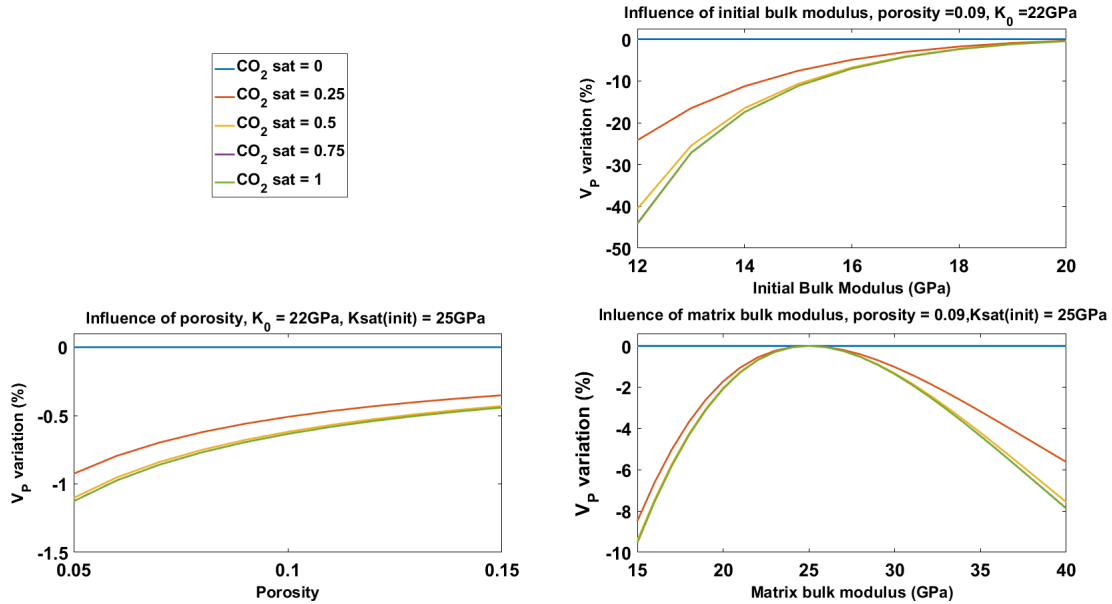


FIG. 15. Influence of  $K_0$ ,  $K_{sat,init}$  and  $\phi$  on the variation in P-wave velocity, for different saturation of  $\text{CO}_2$ .

The effect of the initial bulk modulus, the matrix bulk modulus and of the fluid bulk modulus does not influence the variation of density or the variation of  $V_S$  (equations 1 and 3).

*Final results*

Table 2 resumes the variation of the elastic parameters for 1 year and 5 years of injection and using the Brie and Reuss method to compute the fluid bulk modulus. As mention before, the variation is more important using the Reuss method.

Figure 16 shows the variation of the different elastic parameters after 5 years of injection, using Brie method. The average decrease in P-wave velocity in the plume volume is 2.415%. However, this decrease can reach 15% around the base of the reservoir. This important variation at the bottom of the reservoir was explained in the previous section

The average decrease of density is approximately 0.3% (because part of the brine is replaced by  $\text{CO}_2$  which have a lower density). This decrease in density induces a increase in S-wave velocity (see equation 3) of approximately 0.15%.

Table 2. Average elastic parameters variation.

	1 year of injection		5 years of injection	
	Reuss	Brie	Reuss	Brie
$V_P$ variation (%)	-4.52	-1.82	-5.31	-2.45
$V_S$ variation (%)	0.12		0.15	
Density variation (%)	-0.23		-0.3	

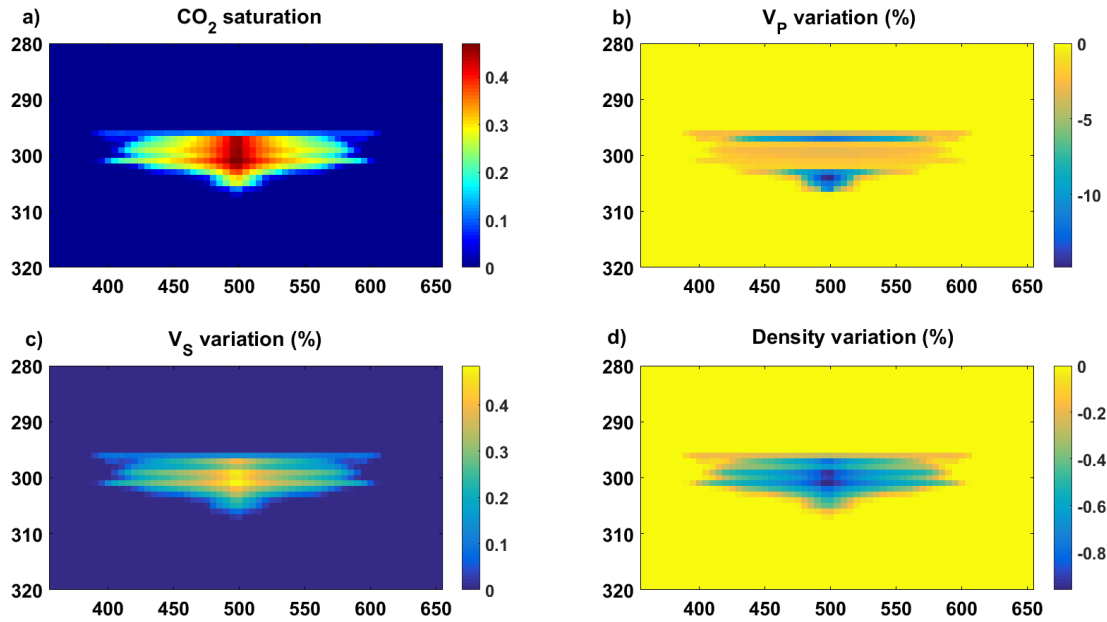


FIG. 16. 2D sections showing the variation of elastic parameters after 5 years of CO<sub>2</sub> injection, for the bottom hole pressure set to 5.8 MPa, reservoir temperature of 20°C. a) rescaled CO<sub>2</sub> saturation, b) P-wave velocity change (%), c) S-wave velocity change (%), d) density change (%).

## FEASIBILITY STUDY OF TIME-LAPSE SEISMIC MONITORING

### Data simulation and processing

Figure 17 shows the survey configuration used for simulate the seismic response due to the gas injection. It corresponds to the inner part of the actual 3C-3D seismic survey acquired in 2014 on the field (Lawton et al., 2015a). It contains a total of 561 receivers and 561 sources, for a final bin size of 5mx5m. The seismic response was simulate for 3 different times:

- the baseline, before CO<sub>2</sub> injection.
- after 1 year of injection (see plain black line on Figure 17) where the medium contains 266 tons of gas.
- after 5 years of injection (see dotted line on Figure 17) where the medium contains 1330 tons of gas.

We use Tiger (SINTEF Petroleum Research) which is a 3D finite-difference modeling software to simulate the seismic synthetic data. The source used is a Ricker wavelet, 40Hz of dominant frequency, the sampling rate is  $4ms$  and the signal length simulated is  $0.748s$  (for an average P-wave velocity of  $2800m.s^{-1}$  and a model thickness of  $500m$ ).

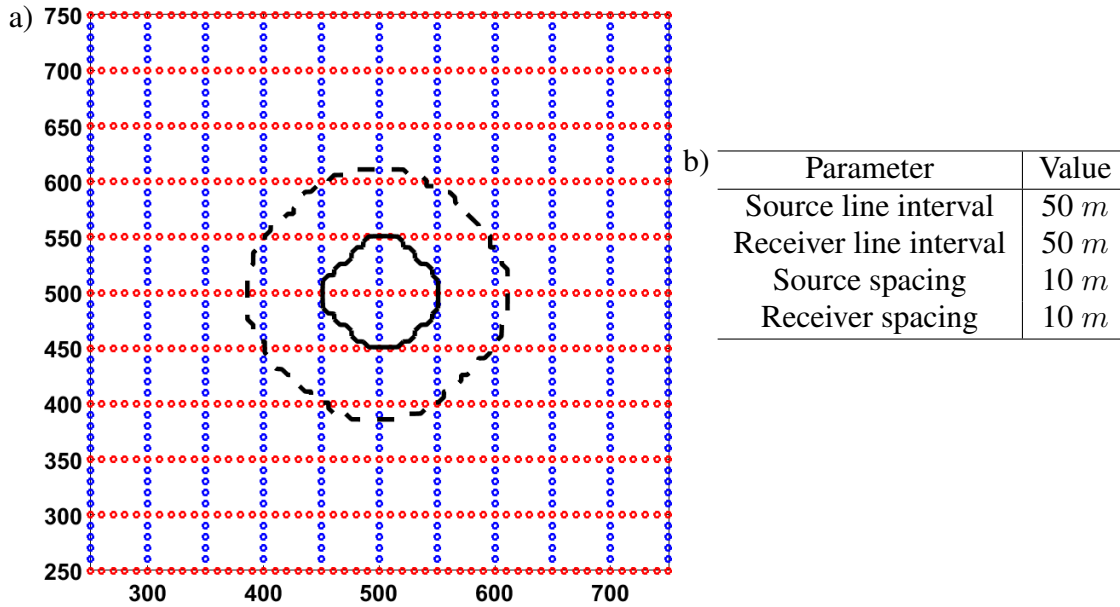


FIG. 17. Acquisition parameters for seismic simulation. a) Blue circles are receivers ; red circles are sources. b) Summary table.

## Results

Figure 18 shows the vertical and horizontal 2D sections on the 3D volume of the difference of the seismic response between 1 year of injection and the baseline (top) and between 5 years of injection and the baseline (bottom). On the vertical sections, the reflectivity anomalies correspond well to the lateral dimension of the gas plume (black lines). The horizontal sections are taken for two-way travel time  $twt = 0.21s$ . The mean velocity is  $2800 m.s^{-1}$ , the corresponding depth is  $294m$  which is the top of the reservoir. The anomaly on the seismic response is well contained inside the CO<sub>2</sub> plume (black contour).

We can note that the amplitude of the anomaly is weaker for 1 year of injection due to the smaller amount of gas in the subsurface and the smaller variation in the elastic parameters.

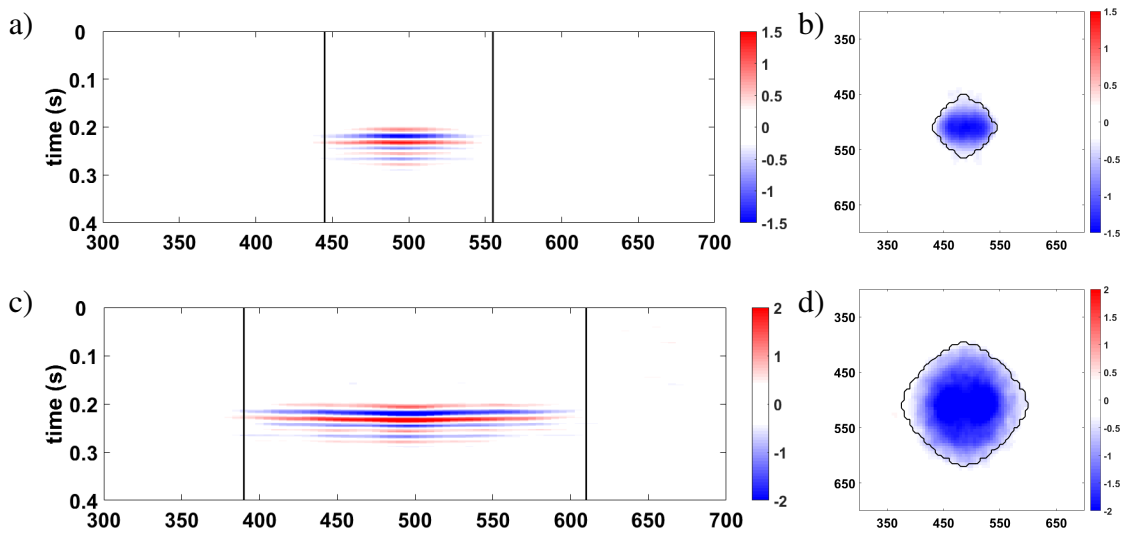


FIG. 18. Results of the difference between the simulated time lapse periods and the baseline seismic volumes. a) Vertical section along the injector well, for 1 year of injection. b) Horizontal section at the top of the reservoir, for 1 year of injection. c) Vertical section along the injector well, for 5 years of injection. d) Horizontal section at the top of the reservoir, for 5 years of injection. Black lines show the lateral expansion of the CO<sub>2</sub> plume.

## From synthetic data to realistic data

The results presented in the previous section are perfect synthetic data without noise, which unfortunately are impossible to reach with real data. We estimate the noise on the real data acquired on the field (Isaac and Lawton, 2015) and add a corresponding random noise on the synthetic seismic response. Signal to noise ratio (SNR) was estimated to be 20 on the real data, we test here this value of SNR (Figure 19) but also a worst scenario where the SNR is 10 (Figure 19). Note that no processing was made to try to reduce the noise.

On Figures 19 and 20, seismic anomaly still correspond to the plume dimension. However, it started to be difficult to distinguish well the reflectivity anomaly for 1 year of injection and SNR=10 (20.a and b). We can notice that the amount of noise is reducing with the depth.

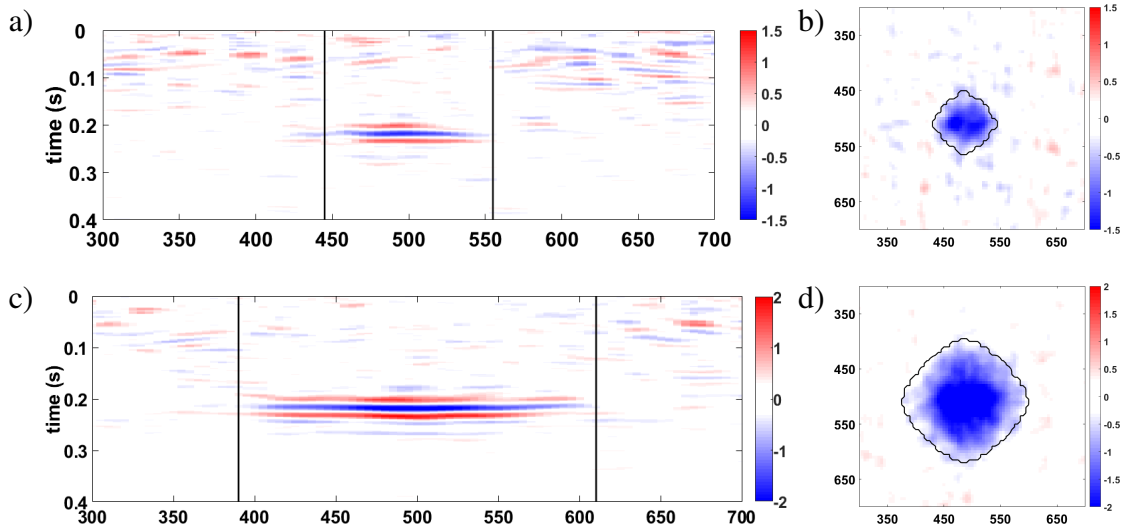


FIG. 19. Results of the difference between the simulated time lapse periods and the baseline seismic volumes, SNR = 20. a) Vertical section along the injector well, for 1 year of injection. b) Horizontal section at the top of the reservoir, for 1 year of injection. c) Vertical section along the injector well, for 5 years of injection. d) Horizontal section at the top of the reservoir, for 5 years of injection. Black lines show the lateral expansion of the CO2 plume.

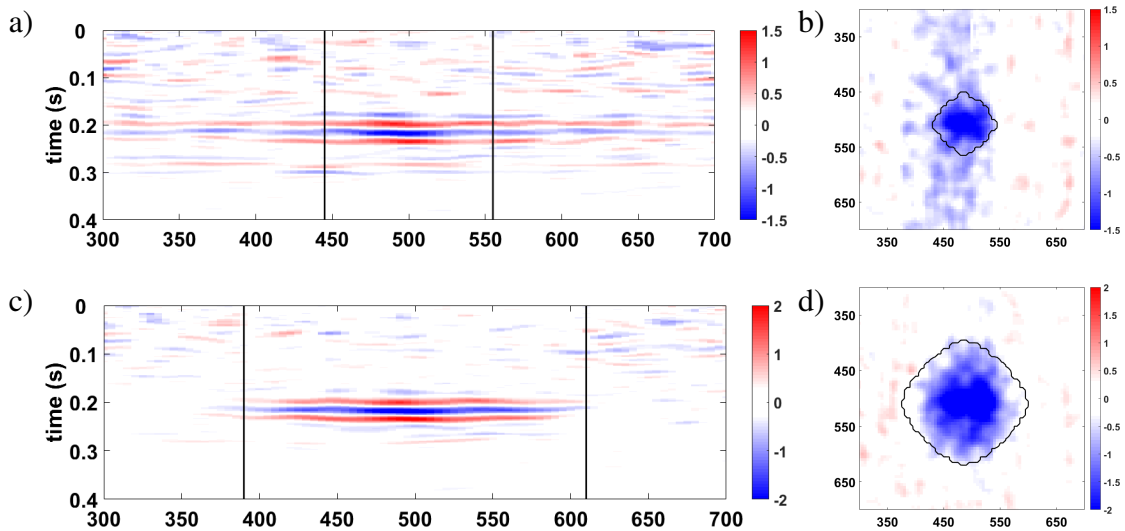


FIG. 20. Results of the difference between the simulated time lapse periods and the baseline seismic volumes, SNR = 10. a) Vertical section along the injector well, for 1 year of injection. b) Horizontal section at the top of the reservoir, for 1 year of injection. c) Vertical section along the injector well, for 5 years of injection. d) Horizontal section at the top of the reservoir, for 5 years of injection. Black lines show the lateral expansion of the CO2 plume.

Note that this seismic simulations are made using the Reuss equation to compute the fluid bulk modulus. Carcione et al. (2006) advise to use the Brie equation, which will reduce the  $V_P$  variation (Table 2), and may induce changes in the recovering of the gas plume.

## WORK IN PROGRESS AND FUTURE WORK

### 4D repeatability

The success of 4D monitoring depends on measuring changes of the elastic parameters due to gas injection. It depends on the ability to produce repeatable measurements between two different periods of time. A good repeatability is a function of the geometry survey (receivers and shots locations), the wavelet and noise conditions as well as the processing applied on the data (for a complete discussion on repeatability, see chapter 4 in Calvert (2005) or chapter 5 in Johnston (2013)). In the previous section we estimated the level of noise on the data acquired on the field (from (Isaac and Lawton, 2015)) and applied that random noise to the synthetic data to getting closer from the reality. However, we did not take into account the error that can be induced by not using the exact same survey configuration.

The non-repeatability between two traces ( $T_1$  and  $T_2$ ) can be measured using the normalized root-mean-square difference (NMRS, eq. 16) on a defined time gate  $t$ .

$$NRMS = \frac{2 * rms(T_{1t} - T_{2t})}{rms(T_{1t}) + rms(T_{2t})} \quad (16)$$

This value quantifies the similarity between two traces, if  $NRMS=0$ , they are identical, if  $NRMS = 2$ , they are exact opposite. A change in the survey geometry can induced a time shift in the traces which will induce an increase in the  $NRMS$ . At a frequency  $f$  and for a time shift of  $dt$  for a sine wave,  $NRMS(f, dt) = 2\pi f dt$ . For example, a time shift of  $1ms$  at a period of  $50Hz$  will give a  $NRMS$  of 0.31 or a non-repeatability of 30% (Calvert, 2005).

This year, a permanent array of 10 by 10 geophones (spacing of 10m, buried at 1m depth) was installed on the field. In July and October, surveys were acquired using this array using the Hawk system (Bertram, 2017). They are both baselines so no changes are expected in the subsurface and can help to characterize the 4D repeatability at CaMI.FRS.

### Monitoring using ambient noise correlation

Ambient noise correlation is now widely used for crustal tomography purposes (Macquet et al. (2014) among a lot of others). The main advantage of this technique is that it does not need punctual sources as earthquakes or man-made sources. The principle is that you can reconstruct the Green function between two station by correlating the continuous signal of these two stations (Figure 21.a). In other words, correlating the continuous signal between two stations allows us to recover the signal registered at one one station if a dirac is shot at the other station. The results of the correlation depends of the properties of the medium between the two stations. If you change the elastic properties of the medium, the result of the correlation will also change (Figure 21.b).

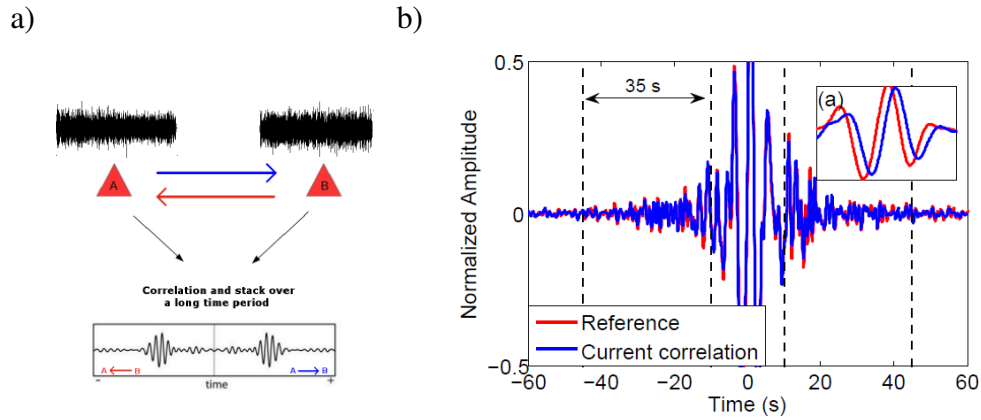


FIG. 21. a) Principle of noise correlation. b) Reference correlation function (blue) and 'current' correlation function (red). Inset (a) shows the time delay of the 'current' correlation function. From Obermann (2013)

From this affirmation emerged the idea of using the ambient noise correlation (also called interferometry) for monitoring purposes. So far, this method was applied on volcanoes (Brenquier et al., 2016), on geothermal site (Obermann et al., 2015) and a feasibility study was done the Ketzin CO<sub>2</sub> storage field (Boullenger et al., 2015).

Lecocq et al. (2014) developed a Python package for monitoring seismic velocity changes using ambient noise. Basically, you choose the processing you want to apply to the data and the software compute the ambient noise correlations. The correlations coefficient between daily correlation and a reference correlation can be measured. If the correlation coefficient is equal to 1, there is no change in the medium (daily correlation and reference correlation are the same); a correlation coefficient less than 1 means that we face a change in the medium which induces a change in the correlation (see an application of this method on a volcano on Figure 22).

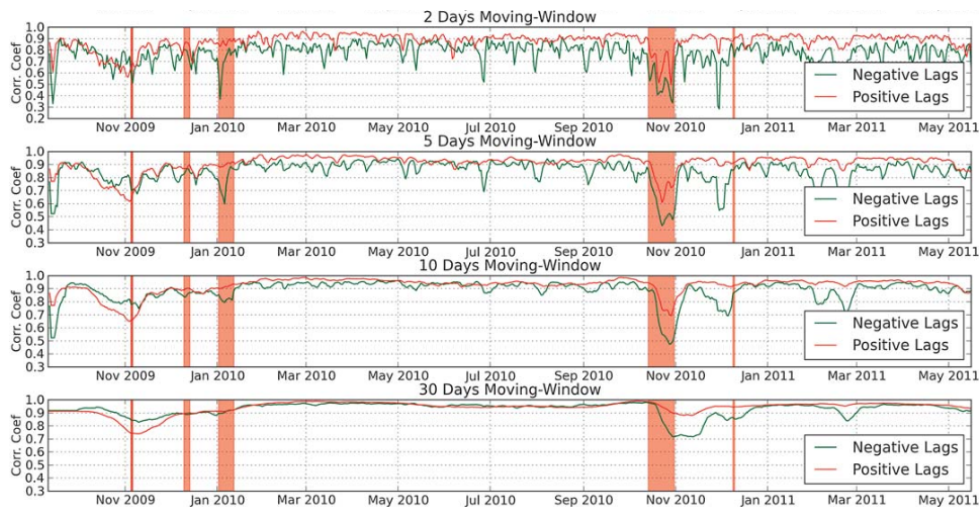


FIG. 22. Variation of correlation coefficients through time for two random stations (YA.UV02 and YA.UV05) of the UnderVolc project . The reference correlation is a stack of all data available. Correlation coefficients are determined by comparing different moving-window stacks to the reference (2, 5, 10 or 30 days). Eruptions of the Piton de la Fournaise are shown as red vertical bands. From Lecocq et al. (2014).

We have a permanent 10x10 geophones installed at CaMI.FRS, which already record some 3 weeks of continuous data (July and October 2017). We can apply the method explained above on these data. No major changes in the correlations are expected because we does not expect major change in the medium. However, it was already demonstrated that change in temperature affect the correlation of ambient noise, as well as the man-made noise. We can see if we can detect, for example, the days the field was 'busy' (seismic shots for example) from the days which it was 'quiet'.

One future plan is that we can record continuously the signal (ambient noise) and vary the injection parameters (pressure for instance). We can determine if we are able to see any changes in the correlation of a pair of stations close to the injector well compare to a pair of station far from the injection well (see Figure 23.a for an example of this application on the St. Gallen geothermal site).

For a more long term objective, we can plan to do imaging of the subsurface using ambient noise, before and after several months of injection. We have the chance to have a dense array of geophone permanently installed which can allow us to have a quit high-resolution image of the subsurface (see Figure 23.b for an example of this application on a volcano).

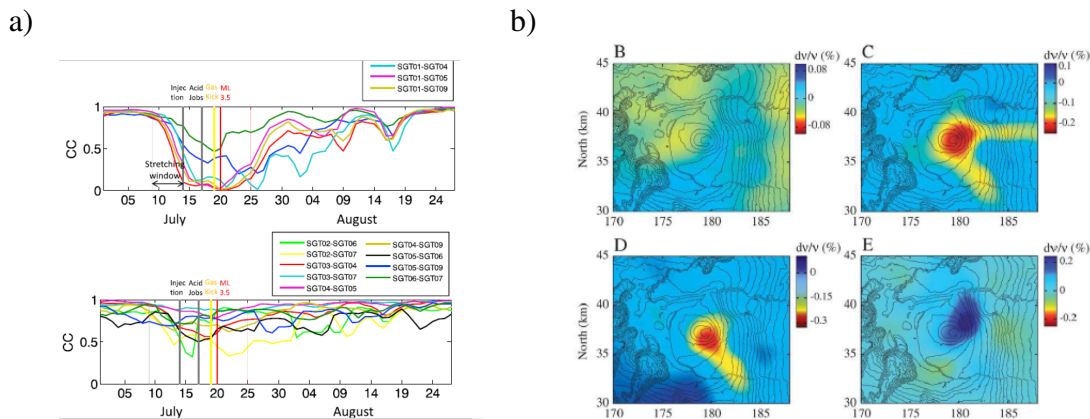


FIG. 23. a) Observed waveform coherence (CC) for the indicated station pairs. Top: close to the injections. Bottom: further away from the injections. The vertical lines in the CC plots mark the injection tests, the gas kick and the ML3.5 earthquake. From Obermann et al. (2015). b) Regionalization of temporal changes.  $dv/v$  are obtained using the stretching technique. (B), period without eruption or cyclones. (C), July 2006 pre-eruptive period. (D), August 2006 pre-eruptive phase. (E), August 2006 post-eruptive period. From Duputel et al. (2009).

## CONCLUSIONS

The feasibility study of seismic monitoring is based on modelings and assumptions. We demonstrate in the injection simulation part that the unknown parameter (vertical over horizontal permeability) can affect the amount of CO<sub>2</sub> you can inject but also the shape of the gas plume (823 tons of CO<sub>2</sub> for a vertical expansion of 11m for  $k_v/k_h = 0.1$  and 1192 tons of CO<sub>2</sub> for a vertical expansion of 24.5m for  $k_v/k_h = 1$ ).

In the second part, we show that the fluid substitution contains also incertitude, mainly on the way to compute the fluid bulk modulus. The interaction between the gas and the brine (uniform saturation, patchy saturation, semi-patchy saturation...) is still not really well known and is really case-dependent. Using an uniform saturation or a semi-patchy saturation can change the average of the variation in P-wave velocity from -5.31% to -2.45%.

Finally, we demonstrate that, using a uniform saturation for the gas fluid substitution, we are able to recover the gas plume in the synthetic seismic data, even with adding random noise to them.

This work is a living work. It was updated when new data were acquired and will be updated in the future, with the start of the injection. The data collected, as pressure, temperature, geochemical and geophysical responses help us to better understand the physics behind the CO<sub>2</sub> sequestration. CaMI.FRS is a unique opportunity to work with different methods from all the Geosciences domains but also develop new technologies to detect and monitor gas migration, and in a bigger-scale to better understand this process and to help de-risk the CCS.

## ACKNOWLEDGEMENTS

We thank CMC and the CREWES sponsors for their financial support. We also gratefully acknowledge support from NSERC (Natural Science and Engineering Research Council of Canada) through the grant CRDPJ 461179-13. We also thank SINTEF for providing access to the TIGER modeling software; Schlumberger for Vista processing software; and CMG for reservoir simulation software. We thank Jessica Dongas and Jacky Barazza for providing the geostatic models used in this study.

## REFERENCES

- Arts, R., Chadwick, A., Eiken, O., Thibeau, S., and Nooner, S., 2008, Ten years' experience of monitoring CO<sub>2</sub> injection in the Utsira Sand at Sleipner, offshore Norway: First break special topic CO<sub>2</sub> sequestration, **26**.
- Barraza, J., 2016, Static model - geomodel upgraded: PPT Presentation - CMC Research Institutes, Inc.
- Batzle, M., and Wang, W., 1992, Seismic properties of pore fluids: *Geophysics*, **57**, No. 11, 1396–1408.
- Bertram, K. L., 2017, Field acquisition in 2017: CREWES Research Report, **this volume**.
- Boullenger, B., Verdel, A., Paap, B., Thorbecke, J., and Draganov, D., 2015, Studying CO<sub>2</sub> storage with ambient-noise seismic interferometry: A combined numerical feasibility study and field-data example for ketzin, germany: *Geophysics*, **80**, No. 1.

- Brenguier, F., Rivet, D., Obermann, A., Nakata, N., Boué, P., Lecocq, T., Campillo, M., and Shapiro, N., 2016, 4-d noise-based seismology at volcanoes: Ongoing efforts and perspectives: *Journal of Volcanology and Geothermal Research*, **321**, 182–195.
- Calvert, R., 2005, *Insights and Methods for 4D Reservoir Monitoring and Characterization: Distinguished Instructor Short Course*, EAGE - SEG.
- Carcione, J. M., Picotti, S., Gei, D., and Rossi, G., 2006, Physics and seismic modeling for monitoring CO<sub>2</sub> storage: *Pure and Applied Geophysics*, **163**, 175–207.
- Dongas, J. M., 2016, *Development and characterization of a geostatic model for monitoring shallow CO<sub>2</sub> injection: Master Thesis*, University of Calgary.
- Duputel, Z., Ferrazzini, V., Brenguier, F., Shapiro, N., Campillo, M., and Nercessian, A., 2009, Real time monitoring of relative velocity changes using ambient seismic noise at the piton de la fournaise volcano (la Réunion) from january 2006 to june 2007: *Journal of Volcanology and Geothermal Research*, **184**, 164–173.
- Gassmann, F., 1951, Über die elastizität poröser medien: *Vierteljahrsschrift der naturforschenden Gesellschaft in Zürich*, **96**, 1–23.
- Gordon, A., and Lawton, D. C., 2017, Zero offset VSP processing of fiber optic cable (DAS) and geophone array at the caMI field research station: *CREWES Research Report*, **this volume**.
- Gordon, A., Lawton, D. C., and Eaton, D. W., 2016, VSP azimuthal travel time analysis at the field research station near brooks, alberta: *CREWES Research Report*, **28**.
- Hall, K. W., Isaac, J. H., Wong, J., Bertram, K. L., Bertram, M. B., Lawton, D. C., Bao, X., and Eaton, D., 2015, Initial 3C-2D surface seismic and walkaway VSP results from the 2015 Brooks SuperCable experiment: *CREWES Research Report*, **27**.
- Hall, K. W., Lawton, D. C., Daley, T., Freifeld, B., and Cook, P., 2017, Source distance and source effort on das data: *CREWES Research Report*, **this volume**.
- Isaac, J. H., and Lawton, D. C., 2015, 3D3C seismic data at the Brooks experimental CO<sub>2</sub> injection site: *CREWES Research Report*, **27**.
- Isaac, J. H., and Lawton, D. C., 2017, A summary of surface seismic reflection data acquired at the field research station near brooks, alberta: *CREWES Research Report*, **this volume**.
- Johnson, D., 2001, Theory of frequency dependent acoustics in patchy-saturated porous media: *Journal of Acoustical Society of America*, **110**.
- Johnston, D. H., 2013, *Practical Applications of Time-Lapse Seismic data: Distinguished Instructor Short Course*, EAGE - SEG.
- Lawton, D. C., Bertram, M., Bertram, K., Hall, K., and Isaac, H., 2015a, A 3C-3D seismic survey at a new field research station near Brooks, Alberta: *CREWES Research Report*, **27**.
- Lawton, D. C., Bertram, M., and Bertram, K. H. K., 2015b, New approaches to seismic monitoring at the Brooks Field Research Station: *CREWES Research Report*, **27**.
- Lawton, D. C., Bertram, M., Hall, K. W., Bertram, K. L., and Macquet, M., 2016, Near-surface velocity characterization at priddis and installation of fibre-optic cables at brooks, alberta: *CREWES Research Report*, **28**.
- Lawton, D. C., Bertram, M. B., Saeedfar, A., and Macquet, M., 2017, DAS installations at the caMI field research station: *CREWES Research Report*, **this volume**.
- Lecocq, T., Caudron, C., and Brenguier, F., 2014, Msnoise, a python package for monitoring seismic velocity changes using ambient seismic noise: *Seismological Research Letters*, **85**, No. 3, 715–726.

- Macquet, M., Paul, A., Pedersen, H., Villaseñor, A., Chevrot, S., Sylvander, M., and Wolyniec, D., 2014, Ambient noise tomography of the Pyrenees and the surrounding regions: inversion for a 3-D Vs model in the presence of a very heterogeneous crust: *Geophysical Journal International*, **199**, No. 1, 402–415.
- Obermann, A., 2013, Monitoring the elastic properties of the crust: numerical analysis and applications using ambient seismic noise: Ph.D. thesis, ISTerre (Institut des Sciences de la Terre).
- Obermann, A., Kraft, T., Larose, E., and Wiemer, S., 2015, Potential of ambient seismic noise techniques to monitor the st. gallen geothermal site (switzerland): *Journal of Geophysical Research: Solid Earth*.
- Rock, L., Brydie, J., Jones, D., Perkin, J.-P., and Taylor, E., 2015, Methodology to assess groundwater quality during CO<sub>2</sub> injection at the Quest CCS project: *Geoconvention, Geoscience New Horizons*.
- Saeefar, A., Macquet, M., Lawton, D. C., and Osadetz, K. G., in prep., Reservoir simulation of CO<sub>2</sub> injection process at the field research station (FRS): phase 1: CMC Research Institutes, Inc. Technical report, 0.
- Spakman, T. W., and Lawton, D. C., 2017, Seismic monitoring with continuous seismic sources: *CREWES Research Report*, **68**.
- Swager, L., 2015, Geophysical log descriptive report: CMCR I COUNTESS 10-22-17-16 ELAN: Schlumberger Carbon Services-CS1512-112-LS, , No. 2.
- Zaluski, W., Lee, S.-Y., and Dongas, J., 2016, Carbon Management Canada static and dynamic model report: Schlumberger Carbon Services-CS1603-020-WZ, , No. 2.